



## Article

# Paleostress Analysis in the Northern Birjand, East of Iran: Insights from Inversion of Fault-Slip Data

Maryam Ezati <sup>1</sup>, Ahmad Rashidi <sup>2</sup> , Ebrahim Gholami <sup>1</sup>, Seyed Morteza Mousavi <sup>1</sup>, Majid Nemati <sup>3</sup>, Shahram Shafieibafti <sup>4</sup> and Reza Derakhshani <sup>4,5,\*</sup> 

<sup>1</sup> Department of Geology, University of Birjand, Birjand 97174-34765, Iran

<sup>2</sup> Department of Seismotectonics, International Institute of Earthquake Engineering and Seismology, Tehran 19537-14453, Iran

<sup>3</sup> Department of Geology, Faculty of Science and Earthquake Research Center, Shahid Bahonar University of Kerman, Kerman 76169-13439, Iran

<sup>4</sup> Department of Geology, Faculty of Sciences, Shahid Bahonar University of Kerman, Kerman 76169-13439, Iran

<sup>5</sup> Department of Earth Sciences, Utrecht University, 3584 CB Utrecht, The Netherlands

\* Correspondence: r.derakhshani@uu.nl

**Abstract:** This research assessed stress regimes and fields in eastern Iran using fault-slip data and the tectonic events associated with these changes. Our stress analysis of the brittle structures in the Shekarab Mountains revealed significant changes in stress regimes from the late Cretaceous to the Quaternary. Reconstructing stress fields using the age and sense of fault movements showed that during the late Cretaceous, the direction of the maximum horizontal stress axes ( $\sigma_1$ ) under a compressional stress regime was  $\sim N290^\circ$ . This stress regime led to the uplifting of ophiolites and peridotites in eastern Iran. During the Eocene, the  $\sigma_1$  direction was NE-SW. The late Eocene and Oligocene stress states showed two distinct transpression and transtension stress regimes. This transition from transpression to transtension in the eastern Shekarab Mountains was the consequence of regional variations in stress regimes. The Quaternary stress state indicates that the tectonic regime in the Quaternary is strike-slip and the  $\sigma_1$  direction is  $\sim N046^\circ$ , which coincides with the current convergence direction of the Arabia–Eurasia plates. Our paleostress analysis revealed that four distinct stress regimes have been recognized in the area, including compressional, transtensional, transpressional, and strike-slip regimes. Our findings indicated that the diversity of the tectonic regimes was responsible for the formation of a variety of geological structures, including folds with different axes, faults with different mechanisms, and the current configuration of the Sistan suture zone.

**Keywords:** stress regime; paleostress; fault; Sistan suture zone; tectonics; structural geology



**Citation:** Ezati, M.; Rashidi, A.; Gholami, E.; Mousavi, S.M.; Nemati, M.; Shafieibafti, S.; Derakhshani, R. Paleostress Analysis in the Northern Birjand, East of Iran: Insights from Inversion of Fault-Slip Data. *Minerals* **2022**, *12*, 1606. <https://doi.org/10.3390/min12121606>

Academic Editors: Lianguo Wang and Zhaolin Li

Received: 10 October 2022

Accepted: 9 December 2022

Published: 14 December 2022

**Publisher's Note:** MDPI stays neutral with regard to jurisdictional claims in published maps and institutional affiliations.



**Copyright:** © 2022 by the authors. Licensee MDPI, Basel, Switzerland. This article is an open access article distributed under the terms and conditions of the Creative Commons Attribution (CC BY) license (<https://creativecommons.org/licenses/by/4.0/>).

## 1. Introduction

Iran is located in a convergence zone between the Arabian and Eurasian plates (Figure 1). The convergence in Iran is primarily accommodated in the north by Alborz, in the northeast by Kopeh-Dagh, in the southwest and west by Zagros, in the east by NS strike-slip faulting, and in the southeast by Iranian Makran [1–5]. GPS studies show that the deformation in Iran is heterogeneous and different blocks and faults accommodate part of this convergent deformation [6].

The closure of several NeoTethys oceanic domains during the late Cretaceous and early Tertiary is visible in a number of sutures, including NainBaft between Central Iran and Sanan-daj Sirjan, Sistan between Lut and Afghanistan, and Sabzevar between Central Iran and Eurasia. The Sistan Suture Zone (SSZ) is adjacent to the eastern Iranian ranges that trend north-south, close to the border with Afghanistan and Pakistan [7–9].

The closure of several NeoTethys oceanic domains during the late Cretaceous and early Tertiary is visible in a number of sutures, including NainBaft between Central Iran and Sanan-daj Sirjan, Sistan between Lut and Afghanistan, and Sabzevar between Central

Iran and Eurasia. The Sistan Suture Zone (SSZ) is adjacent to the eastern Iranian ranges that trend north-south, close to the border with Afghanistan and Pakistan [7–9].

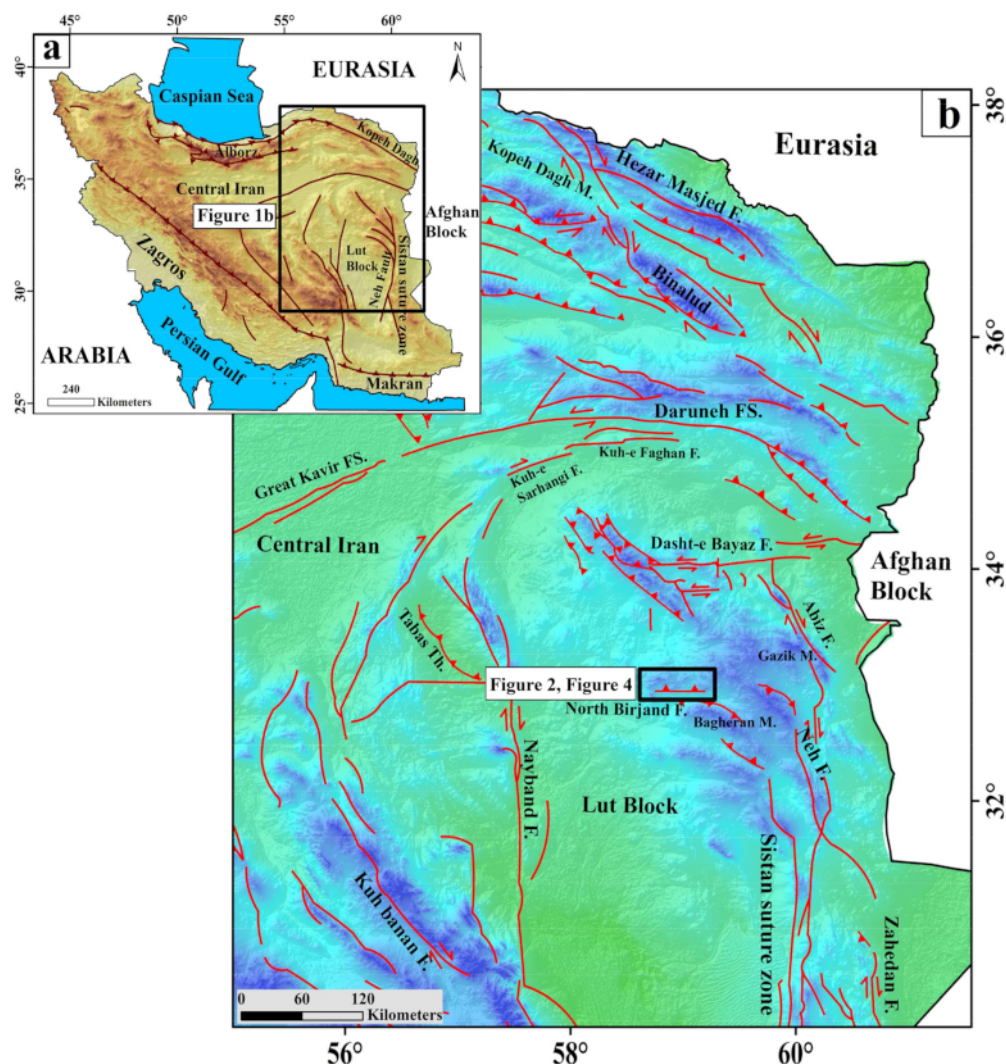


**Figure 1.** (a) Structural zones of Iran and location of eastern Iran (black rectangle); (b) structural map of eastern Iran, the black rectangle indicates the location of the region studied.

The northward movement of central and northern Iran relative to Afghanistan generates a north-south dextral shear of  $\sim 16$  mm/yr along the eastern border [6,10]. Several dextral fault systems bordering the Lut have been formed by the north-south shear between Iran and Afghanistan [11,12]. The Sistan Suture Zone (SSZ), a north-south trending accretionary prism, is overprinted by the Nehbandan fault system at the eastern boundary of the Lut Block. One of the terminal segments of the Nehbandan fault with an E-W sigmoidal trend is thought to be the North Birjand Fault (NBF), which exhibits a sinistral and reverse mechanism [13]. Some N-S strike-slip fault systems, including the Nayband, Gowk, and Sabzevaran, can be found along the western edge of the Lut Block [14,15]. Along these strike-slip faults in eastern Iran, the Lut and Tabas blocks are displaced in accordance with the overall deformation in the Arabia–Eurasia collision zone.

Strike-slip faults are primarily responsible for a number of earthquakes in Iran [16–18], particularly from a morphotectonic and seismotectonic viewpoint [19–21], and play a significant role in the present deformation of eastern Iran. Since the Pliocene, the dominant tectonic mode in the Iranian plateau and surrounding belts has shifted from compressional to strike-slip [22]. Several indicators of tectonic activity, such as the offset of drainages, instrumental seismicity, and paleoseismology on dextral N-S faults and their sinistral conjugates related to

NW-SE reverse faults, indicate that the SSZ has been tectonically active up until the present. Moreover, the northern terminal of the Nehbandan fault system terminates in the NW-SE and E-W thrust faults [12]. What caused the heterogeneous distribution of rock units and increased outcropping of igneous rocks in the eastern part of the Shekarab Mountains is the central question of this study. The present study aims to determine stress regime changes in the E-W trend structures in the SSZ as the eastern border of the Iranian Plate. Therefore, we chose the Shekarab Mountains within SSZ as a case study with an E-W trend, since the faults of this region are well exposed with rock units of different ages.

Furthermore, fault-slip data inversion was utilized to differentiate stress changes in the study area. This research will yield important insight into the evolution of the E-W trending mountain ranges in the SSZ. In this study, the direct stress tensor inversion method [23] was adopted to compute the state of stress. The eastern margin of the Dead Sea [24], Ahar in NW Iran [25], SW Iran [26,27], Cascadia megathrust [28], south-central Vietnam [29], south Poland [30], the eastern margin of the Sichuan Basin, China [31], the western part of Central Iran [32], and the NW lesser Himalayan sequence [33] are some areas of the earth's crust where this type of research has been applied.

## 2. Tectonic Setting

The SSZ demonstrates a deformed accretionary prism that was emplaced during the destruction of a small Neo-Tethys (named the Sistan Ocean). Since the Cretaceous, the SSZ has undergone a rather complex history marked by variations in the tectonic environment and corresponding variations in the stress regime. However, the present configuration of the SSZ is due to the Cenozoic deformation phase, including rifting, subductions, ophiolite emplacement, continental trench collisions, and uplift [8]. The SSZ has been dominated by major N-S or NNW-SSE dextral faults, NW-SE reverse faults, and E-W sinistral faults [8,34,35]. North of 32° N, dextral shear is taken up; furthermore, the strike-slip faults terminate in the thrust faults and their displacement diminishes as they approach their terminations [36]. The Birjand region includes a series of roughly WNW-ESE linear mountain ranges, such as the Shekarab Mountains, Bagharan Mountains, and Gazik Mountains [2,12,37,38]. The mountain ranges uncover the upper Cretaceous to Eocene ophiolite units of the SSZ, which mostly have been cut by inherited faults and shear zones [7]. The southern and northern terminals of the Nehbandan fault system, which is characterized by a dextral mechanism, contain splays. The northern end of this fault has rotated westward, while the southern end has rotated eastward [39]. The Shekarab Mountains are created by one of the northern splays of the Nehbandan fault system and are located north of Birjand (Figure 1). This area includes a complete sequence of rock units in eastern Iran after the Cretaceous, where fault distribution is suitable for paleostress analysis. The E-W Shekarab Mountains is a sinistral transpressional shear zone; its most important structures include pop-ups, duplexes, triangle zones, flower structures, and shear folds. Sedimentary, volcanoclastic, and igneous rocks are the essential outcropping units in the Shekarab Mountains. There is an E-W thrust fault with a sinistral component in the southern front of the Shekarab Mountains, called the North Birjand Fault (N.B.F), which separates the Quaternary units to the south from the older units to the north [2,12]. Four cross-sections of the Shekarab Mountains were drawn to provide a good structural view (Figure 2). In this research, we prepared a geological map and synthetic lithostratigraphic column for the Shekarab Mountains. As shown in Figure 3, units older than the upper Cretaceous have not been identified in this area.



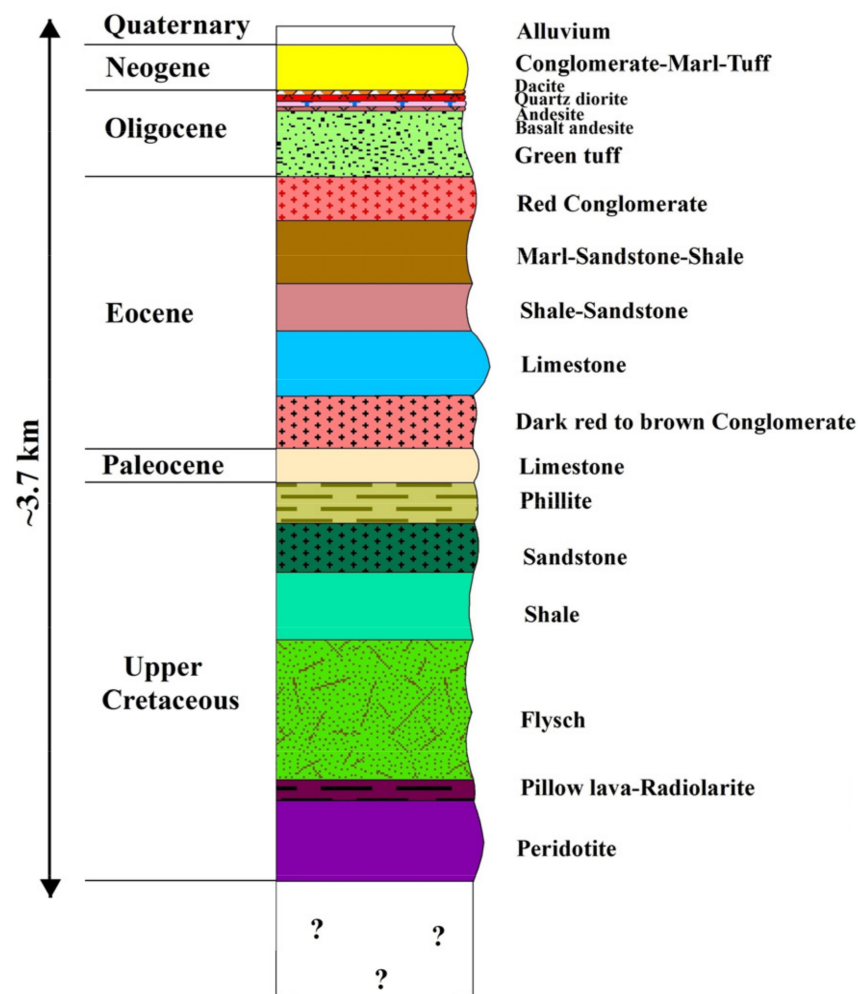


**Figure 3.** Synthetic log of the Shekarab Mountains. Their surface expansion is shown on the geological map of Figure 2.

### 3. Material and Methods

The inversion approach of the fault-slip data is based on a decreased misfit angle ( $\alpha$ ), which is derived as the minimum angle between the computed relative shear stress ( $\tau$ ) and the actual striae ( $s$ ) [40,41]. The technique of stress tensor inversion maximizes the total slip shear stress in the real slip trend for the whole dataset. This total is computed based on four independent variables of the reduced stress tensor, namely the three angular parameters for the direction of the main stress axes,  $\sigma_1 \geq \sigma_2 \geq \sigma_3$ , and the ratio of the main stress magnitude differences, which is defined as:

$$\Phi = (\sigma_2 - \sigma_3) / (\sigma_1 - \sigma_3)$$

The  $\Phi$  ratio gives the shape and orientation of the stress ellipsoid [23]. In the inversion of fault-slip data, an important parameter is the minimum misfit level required for determining good data. This study employed a scale ranging from  $-100\%$ , related to the total misfit, to  $100\%$ , associated with the perfect fit. The lowest range included the maximum shear stress, which acts in the opposite direction of slip. At the highest range, the shear stress was also at its highest level, but it behaves similarly to the slip in both sense and direction. A zero amount of reduced misfit angle indicated the shear stress perpendicular to the slip as the limit between inconsistent and consistent directions of motion [23]. The right-dihedron method, one type of paleostress inversion method, only provides a confidence ellipse that includes two of the main stress axes [42]. All available techniques for stress calculation are based on the stress-shear relationship described by Bott [43]. This method for stress calculation is based on

the stress-shear relationship described by refs. [43,44]. All paleostress inversion methods were developed in accordance with the fundamental assumptions.

The slip that is demonstrated by fault plane striations of a dataset has the sense and orientation of the determined shear stress on each fault surface. The slips on a single fault are not affected by interaction with other faults, which is generally correct for small fault-slips, and each fault-slip corresponds to the single stress tensor.

In the theoretical reviews, evaluations of only four fault-slips are needed to calculate the reduced stress tensor and magnitude of the shear stress on the fault planes, and no technique considers that the quality of stress inversion mainly depends on the field data's quality [45]. Inversion computes a mean best-fitting deviatoric stress tensor from a set of at least four striated faults by minimizing the angular deviation between the predicted slip vector (maximum shear) and the observed striation [46]. To determine the different stress regimes in the Shekarab Mountains, we performed a quantitative inversion of distinct sets of the fault-slip data using the method described by ref. [46]. This method assumes that rigid block displacements are independent. The method described by Carey [46] has also been used by Jentzer et al. [47]. Because the Shekarab Mountains are the same area that Jentzer et al. [47] studied, Carey's approach [42] was used in this research. In all of the inversion methods, the principal hypothesis is that the slip responsible for the striation occurs in the sense and orientation of the shear stress on each fault surface. The stress regime can be determined using the trend of the main stress axes, including the  $\sigma_1$ ,  $\sigma_2$ ,  $\sigma_3$ , and  $\Phi$  ratio; hence, a distinct stress tensor can produce only one slip orientation on a particular fault surface [40,41]. In most fieldwork, more than one generation of slickenlines is found on a fault surface. Often, this is due to creating multiple slips in a single event, variations in slip orientations owing to changes in the local boundary conditions or fault strength, and temporal variations in the regional state of stress due to variations in boundary conditions at the scale of plate tectonics by distinct tectonic regimes have been characterized [41].

In this study, the fault kinematic data, including the orientation of the main fault planes and associated strike, were measured at 37 sites ranging in age from the late Cretaceous to the Quaternary (Figure 4). In order to obtain stress tensor inversion in the study area, the majority of brittle structures, such as the orientation of fault planes, slicken lines, and indicators of the sense of motion, were collected (Table 1). Each fault in Table 1 demonstrates the statistical mean of many collected data points (N is the sum of the number of data on the fault-slips. in Table 2). The dataset was separated into homogeneous subsets to reconstruct different stress fields in order to determine the stress field and stress tensor direction in various geological times. The brittle structures associated with different geological times were separated to determine the orientation of the stress tensor and stress state using Wintensor software [48]. We identified the various stress regimes from the late Cretaceous to the Quaternary using fault-slip stress tensor inversion and brittle tectonics analysis. Here, Right Dihedron and P, B, and T axes methods were used. The Right Dihedron method only gives an estimate of orientations of the  $\sigma_1$ ,  $\sigma_2$ , and  $\sigma_3$  axes. The moment stress axes P, B, and T demonstrate the maximum shortening, unbiased axis, and maximum extension, respectively.

**Table 1.** Geometric–kinematic location of the detected faults in the research area; N.B.F = North Birjand Fault.

Fault Name	Geometric Position (Trend/Plunge)	Slickenline Position (Trend/Plunge)	Fault Mechanism	Location	Latitude (N°) Longitude (E°)
F1	N045, 72NW	N355, 60	Reverse with dextral strike-slip component	Eastern section	33°05′47.58″ 59°16′23.70″
F2	N120, 55NE	N300, 0	Sinistral strike-slip	Eastern section	33°02′30.06″ 59°17′55.98″

Table 1. Cont.

Fault Name	Geometric Position (Trend/Plunge)	Slickenline Position (Trend/Plunge)	Fault Mechanism	Location	Latitude (N°) Longitude (E°)
F3	N340, 67NE	N070, 67	Reverse	Eastern section	33°04'19.20" 59°14'47.10"
F4	N353, 54NE	N129, 43	Reverse with sinistral strike-slip component	Eastern section	33°03'52.02" 59°04'40.56"
F5	N085, 65SE	N247, 18	Sinistral strike-slip with reverse component	Western section	33°02'30.05" 59°02'53.92"
F6	N210, 85NW	N034, 32	Reverse with Sinistral strike-slip component	Western section	33°01'38.34" 58°41'19.44"
F7	N230, 30NW	N290, 25	Reverse with dextral strike-slip component	Western section	33°01'25.62" 58°42'42.90"
F8	N130, 70SW	N192, 67	Reverse with dextral strike-slip component	Western section	33°01'16.56" 58°41'07.92"
F9	N120, 70SW	N134, 37	Dextral strike-slip with reverse component	Western section	33°01'19.14" 58°39'51.24"
F10	N290, 55NE	N059, 47	Reverse with sinistral strike-slip component	Western section	33°01'19.32" 58°39'21.06"
F11	N180, 15W	N210, 64	Reverse with dextral strike-slip component	Western section	33°00'44.22" 58°42'46.98"
F12	N355, 70NE	N148, 50	Reverse with sinistral strike-slip component	Middle section	32°59'15.24" 58°46'46.98"
F13	N310, 32NE	N103, 15	Sinistral strike-slip with reverse component	Middle section	32°55'49.14" 58°51'22.98"
F14	N070, 80NW	N045, 45	Reverse with sinistral strike-slip component	Middle section	32°56'17.28" 58°51'08.46"
F15	N238, 50SE	N040, 8	Sinistral strike-slip with reverse component	Middle section	32°58'17.28" 58°51'08.46"
F16	N035, 65NW	N223, 64	Reverse with dextral strike-slip component	Middle section	32°56'37.20" 58°51'34.74"
F17	N165, 80SW	N310, 25	dextral strike-slip with reverse component	Eastern section	32°54'12.12" 58°52'29.40"
F18	N030, 80SE	N105, 79	Normal with dextral strike-slip component	Eastern section	32°58'19.62" 58°59'32.04"
F19	N090, 70S	N070, 65	Normal with Sinistral strike-slip component	Eastern section	32°58'45.66" 58°59'24.30"
F20	N349, 50NE	N142, 45	Reverse with sinistral strike-slip component	Eastern section	33°00'04.80" 59°00'00.18"
F21	N090, 70S	N133, 62	Reverse with sinistral strike-slip component	Eastern section	32°58'52.32" 59°04'41.04"

Table 1. Cont.

Fault Name	Geometric Position (Trend/Plunge)	Slickenline Position (Trend/Plunge)	Fault Mechanism	Location	Latitude (N°) Longitude (E°)
N.B.F	N80E, 65NW	N036, 55	Reverse with sinistral strike-slip component	Eastern section	33°05′47.58″ 59°16′23.70″
F22	N090, 50S	N092, 70	Reverse with dextral strike-slip component	Eastern section	33°02′30.06″ 59°17′55.98″
F23	N084, 50S	N152, 48	Reverse with dextral strike-slip component	Eastern section	33°04′19.20″ 59°14′47.10″
F4	N165, 75SW	N272, 65	Normal with dextral strike-slip component	Eastern section	33°03′52.02″ 59°04′40.56″

**Table 2.** Reconstructed stress regimes and geological situation of brittle structures. N, number of data on the fault-slips.  $\Phi$ , ratio of stress magnitude differences ( $\Phi = (\sigma_2 - \sigma_3)/(\sigma_1 - \sigma_3)$ ).  $\alpha$ , the average angle between the calculated shear and observed slip in degrees.

Site	N	Stratigraphic Age	$\sigma_1$ Trend, Plunge	$\sigma_2$ Trend, Plunge	$\sigma_3$ Trend, Plunge	$\Phi$	$\alpha$	Location
1	9	Eocene	081, 23	378, 05	246, 64	0.5	18	Eastern section
2	11	Eocene	069, 21	162, 09	273, 67	0.45	10	
3	10	Eocene	067, 21	161, 09	272, 67	0.45	3	
4	12	Eocene	275, 31	014, 15	126, 55	0.79	12	
5	11	Eocene	028, 30	294, 04	198, 57	0.5	17	
6	10	Eocene	221, 00	131, 67	312, 18	0.4	12	
7	13	Eocene	024, 12	289, 22	141, 64	0.5	11	
8	13	Eocene	266, 34	005, 14	115, 52	0.77	7	
9	6	Oligocene	270, 86	180, 00	090, 04	0.31	11	
10	12	Quaternary	220, 07	314, 35	120, 55	0.83	15	
11	12	Quaternary	221, 06	313, 16	112, 73	0.5	11	
12	10	Eocene	034, 01	125, 67	304, 20	0.5	12	
13	12	UP. Cret	280, 08	173, 64	014, 25	0.5	6	
14	12	Paleocene	286, 07	187, 52	021, 37	0.54	4	
15	12	Oligocene	359, 8	189, 52	093, 05	0.52	8	
16	13	Oligocene	008, 60	257, 11	162, 27	0.65	20	
17	6	UP. Cret	143, 23	281, 61	045, 18	0.78	10	
18	12	Eocene	241, 01	151, 01	018, 88	0.71	22	
19	11	Paleocene	307, 11	042, 24	193, 64	0.95	17	
20	30	Eocene	187, 08	095, 11	311, 77	0.64	21	Middle section
21	14	Oligocene	218, 06	313, 34	118, 54	0.8	13	
22	10	Eocene	215, 06	112, 61	306, 24	0.64	5	



Table 2. Cont.

Site	N	Stratigraphic Age	$\sigma_1$ Trend, Plunge	$\sigma_2$ Trend, Plunge	$\sigma_3$ Trend, Plunge	$\Phi$	$\alpha$	Location
23	10	Quaternary	272, 31	015, 3	128, 54	0.69	8	Middle section
24	12	Oligocene	081, 03	348, 38	175, 52	0.21	3	
25	12	Oligocene	244, 05	155, 05	022, 90	0.68	9	
26	5	Quaternary	060, 10	277, 77	152, 08	0.5	13	
27	10	Eocene	207, 02	300, 16	107, 70	0.55	10	
28	10	Quaternary	068, 11	338, 00	246, 79	0.5	11	western section
29	10	Quaternary	064, 04	334, 01	237, 86	0.75	13	
30	13	Eocene	038, 00	308, 20	128, 70	0.5	19	
31	12	Eocene	221, 13	285, 20	139, 62	0.5	15	
32	12	UP. Cret	100, 18	007, 07	257, 71	1	23	
33	10	UP. Cret	157, 26	250, 06	352, 64	0.1	7	
34	9	Eocene	217, 07	113, 63	310, 26	0.67	6	
35	10	Eocene	224, 00	133, 70	314, 20	0.3	8	
36	9	Eocene	036, 00	127, 69	306, 21	0.5	5	
37	10	Eocene	037, 02	132, 63	306, 27	0.5	9	

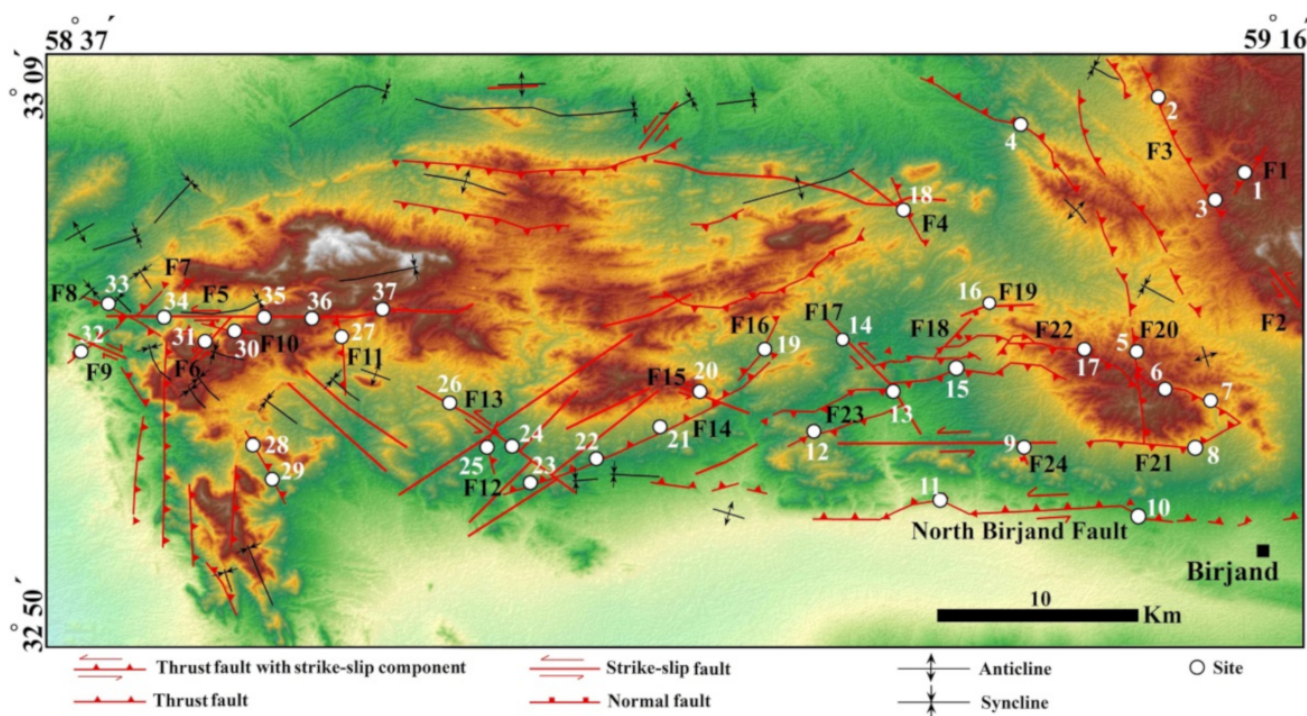
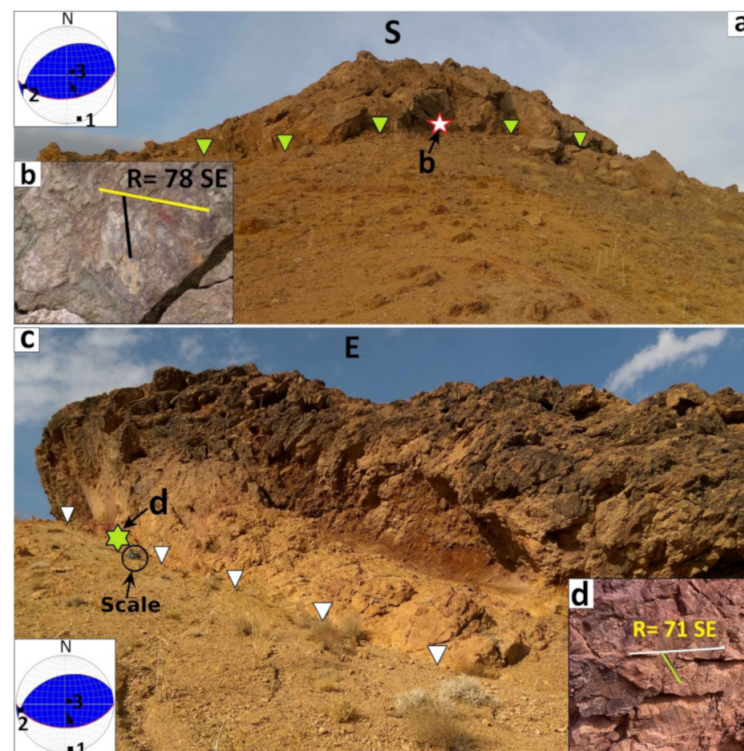


Figure 4. The structural map of the research area and locations of collected paleostress data. F1 to F24 are faults number 1 to faults number 24.

### 3.1. Analyses of Stress Regime Changes

In this paper, for paleostress and structural analysis of the study area, changes in the stress directions from the late Cretaceous to younger periods have been investigated. The strike-slip, thrust, and normal faults were all formed due to the primary compressional stress; geometric–kinematic analyses of these structures showed that almost all faults had a reverse component (Figure 4, Table 1), which emphasized the compressional stress. The

direct inversion method and stress determination revealed a variety of stress regimes and stress directions. The oldest stress state determined in the study area was the late Cretaceous paleostress state. The paleostress state and kinematic history of the Pre-Cretaceous remained unclear. The inversion analysis of late Cretaceous fault kinematics was conducted to validate the stress status. The Cretaceous units were scattered throughout the entire parts of area (site numbers 13, 17, 32, and 33) (Figures 2 and 4). There were two outcrops of the Cretaceous period in the ophiolites and peridotite units (site numbers 13 and 17) (Figure 4). The faults observed in site numbers 13 and 17 were reverse, and the stress regime was compressional. The performance of the compressional stress regime in the eastern portion of the research area resulted in the uplift of ophiolites and peridotites, and the principal stress axis ( $\sigma_1$ ) at sites 13 and 17 was oriented NW–SE. In western parts of the Shekarab Mountains, the data collected from sites 32 and 33, located on the F7 and F8 reverse faults, showed a compressional stress regime. The major stress axis ( $\sigma_1$ ) in site numbers 13, 17, and 32 had an NW–SE direction; also, one outcrop (site number 33) indicated various  $\sigma_1$  directions (Table 2). In the Shekarab Mountains, two outcrops of the Paleocene units existed. The Paleocene data were collected from sites 14 and 19, and inversion of the fault-slip vector indicated that  $\sigma_1$  was oriented toward NW–SE (Table 2). Seventeen outcrops of the Eocene period existed in the sandstone, limestone, conglomerate, and andesite units (Figure 2). The observed faults in the Eocene units were mainly reverse or strike-slip with a reverse component, and the stress regime in this period was purely transpressive (Figure 5). Based on the  $\sigma_1$  direction, two subsets were distinguished: one with  $\sigma_1 \sim N035^\circ$  (site numbers 2, 3, 4, 7, 8, 18, 20, 30, 34, 35, 36, and 37) and one with  $\sigma_1 \sim N315^\circ$  (site numbers 5, 6, 22, and 31), as well as one outcrop exhibiting a different  $\sigma_1$  orientation (site number 27). Moreover, the trend of  $\sigma_1$  in the Eocene was approximately N–S (Table 2).



**Figure 5.** (a) Field photo of F23 fault trace that is reverse with dextral strike-slip mechanism. (b) Slickenside on the minor fault in part. (c) Trace of F22 fault which is reverse with a dextral component. (d) Slickenside on the minor fault in part. Numbers 1, 2, and 3 in the stereonet represent the direction of the main stress axes, while the arrow represents the trend of movement of the hanging wall.

In the Shekarab Mountains, there was evidence of both transtensional and transpressional stress regimes during the Oligocene. The transpressional stress regimes were demonstrated

by compressional sites along the major reverse faults (sites 12, 15, 21, and 25), whereas the transtensional stress regime was controlled by normal faults (site numbers 9 and 16).

Normal faults were found in the area’s eastern section. As a result, transtensional stress regimes were nearly evenly distributed along normal faults, whereas compressional stress regimes were observed throughout the region (Figure 6; Table 2). The data collected from sites 9 and 16 indicated a transtensional stress regime in the eastern section of the area (Figures 6 and 7). The transtensional stress regime was observed in normal faults, including F18, F19, and F25 faults. Moreover, along the F19 and F25 normal faults, two transtensional stress tensors were controlled by fault geometries.

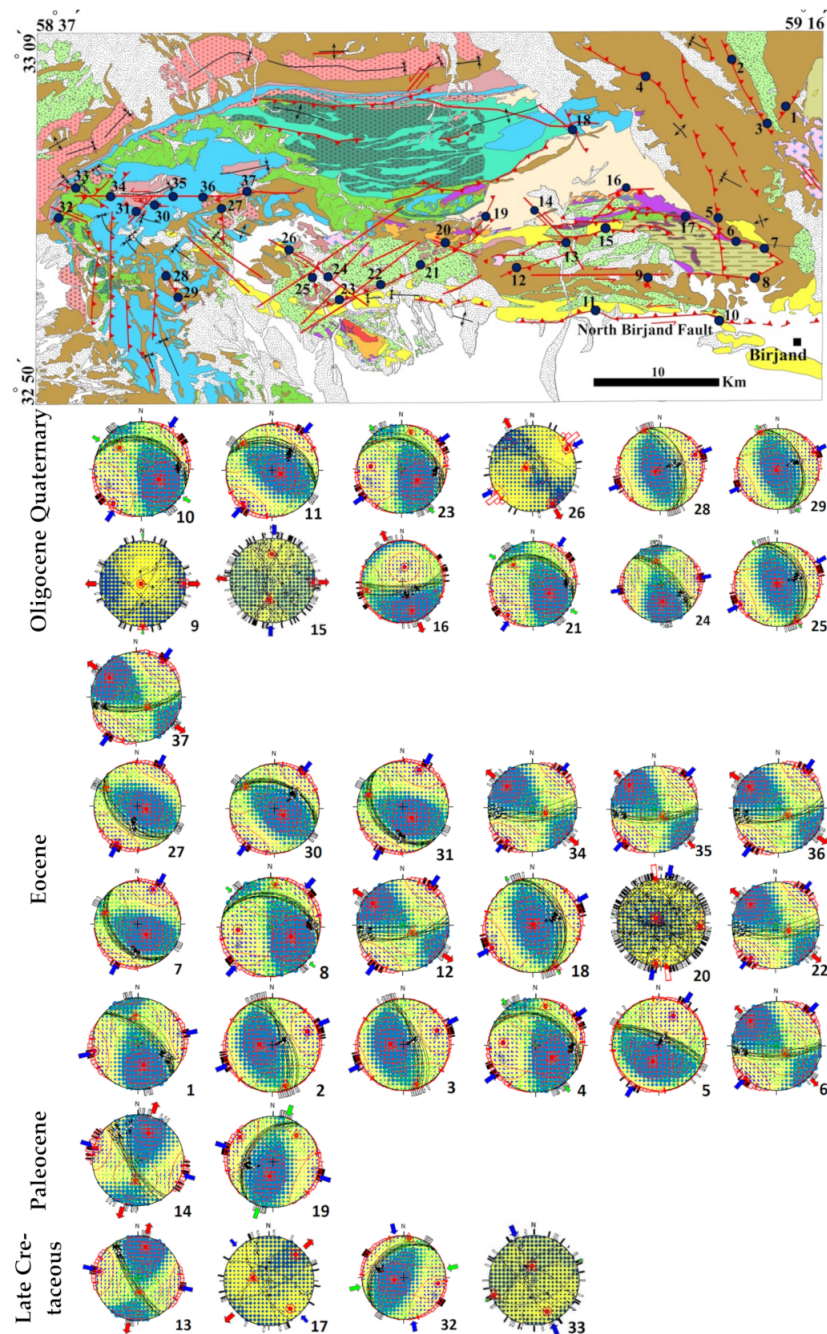
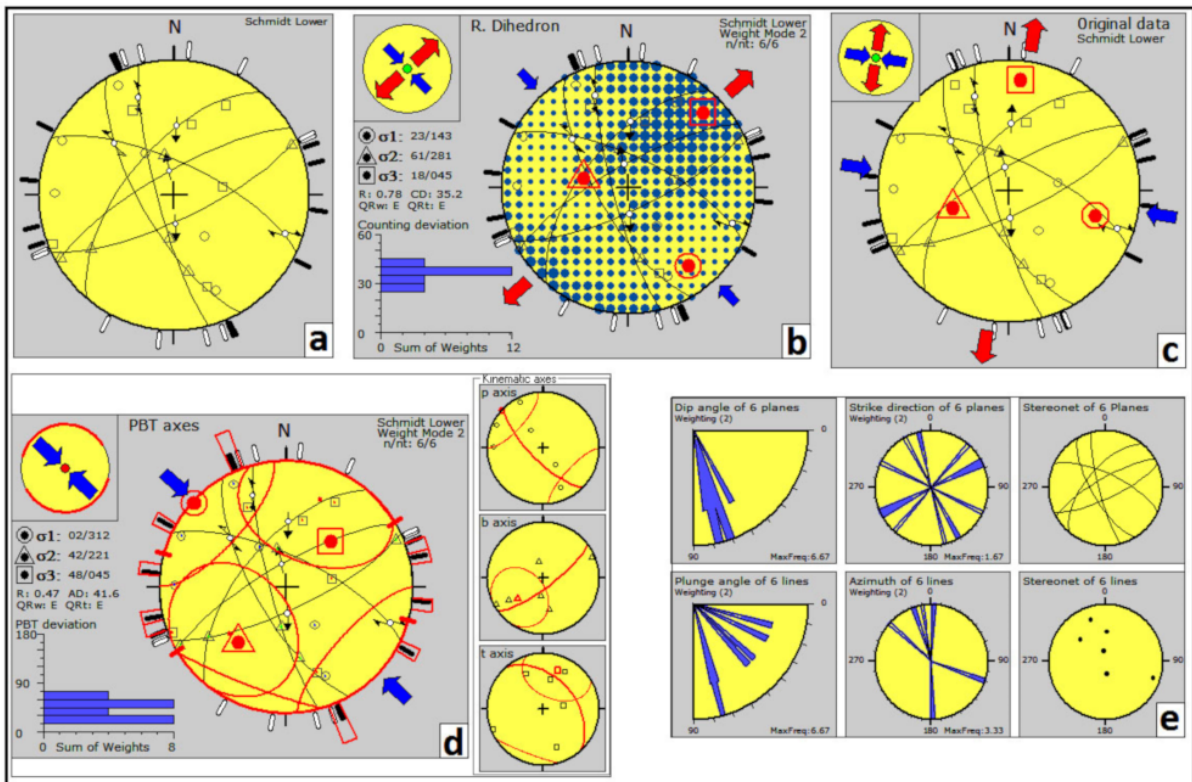


**Figure 6.** Orientation of the main stress axes related to the upper Cretaceous to Quaternary units. The numbers are the numbers of the sites that collected the faults data.

Site 17



Site 20

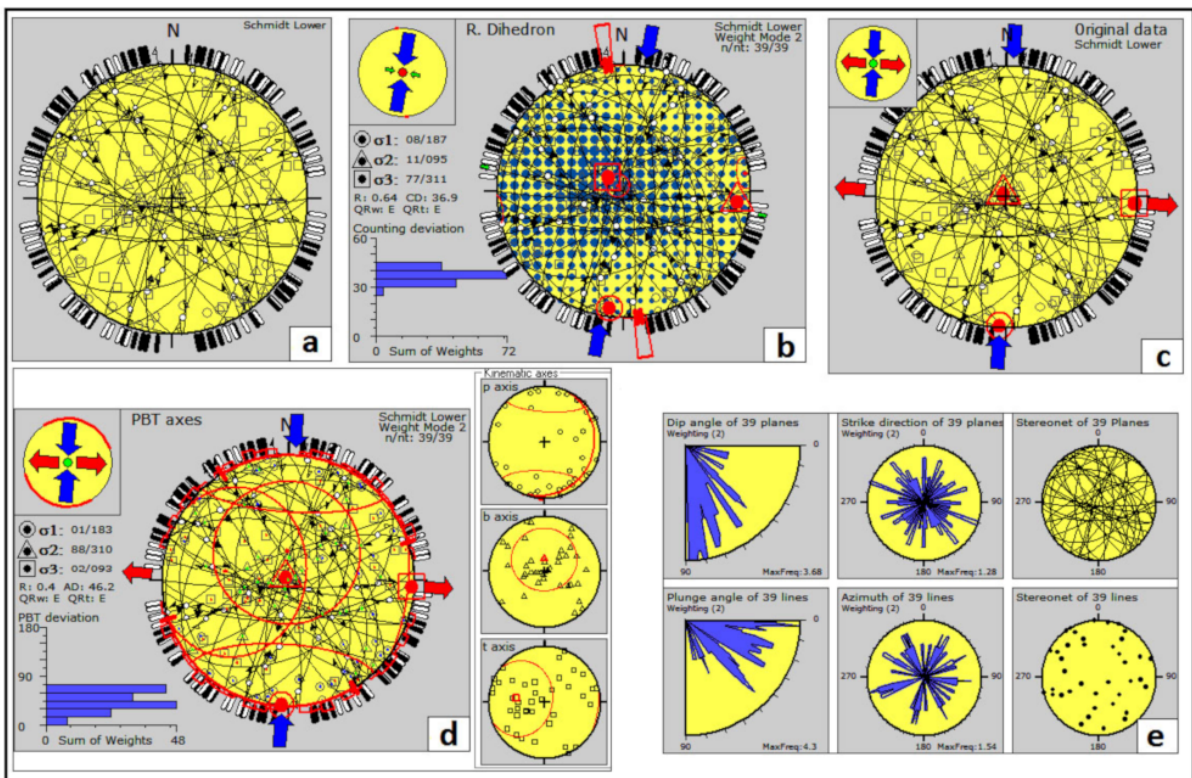
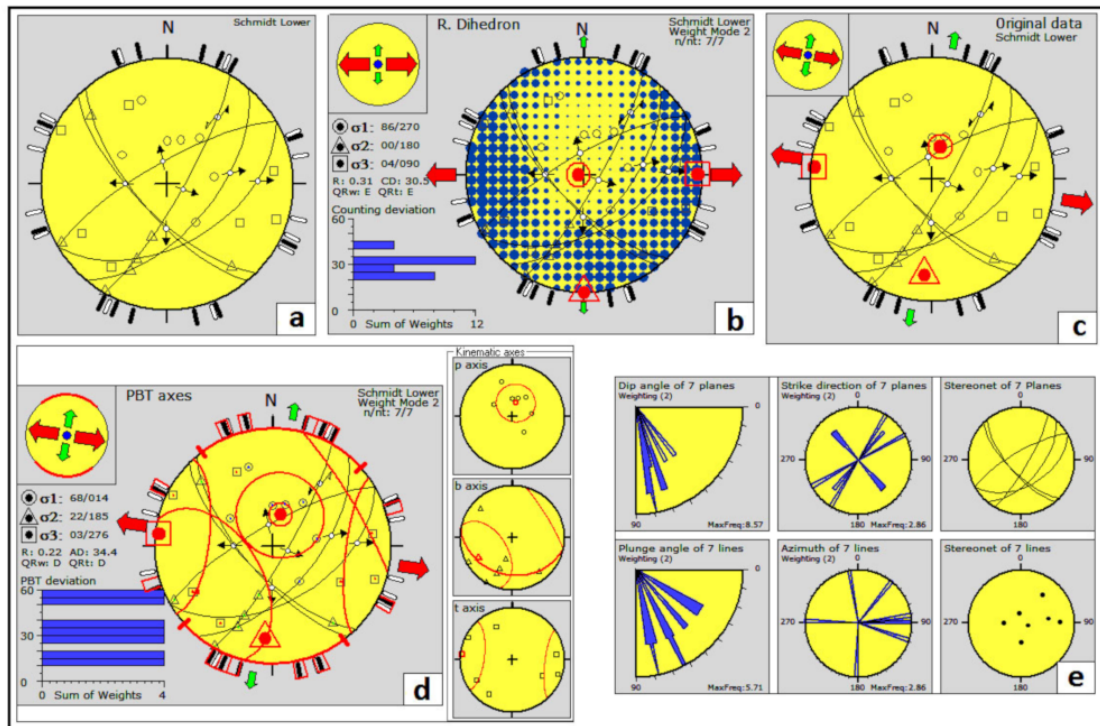
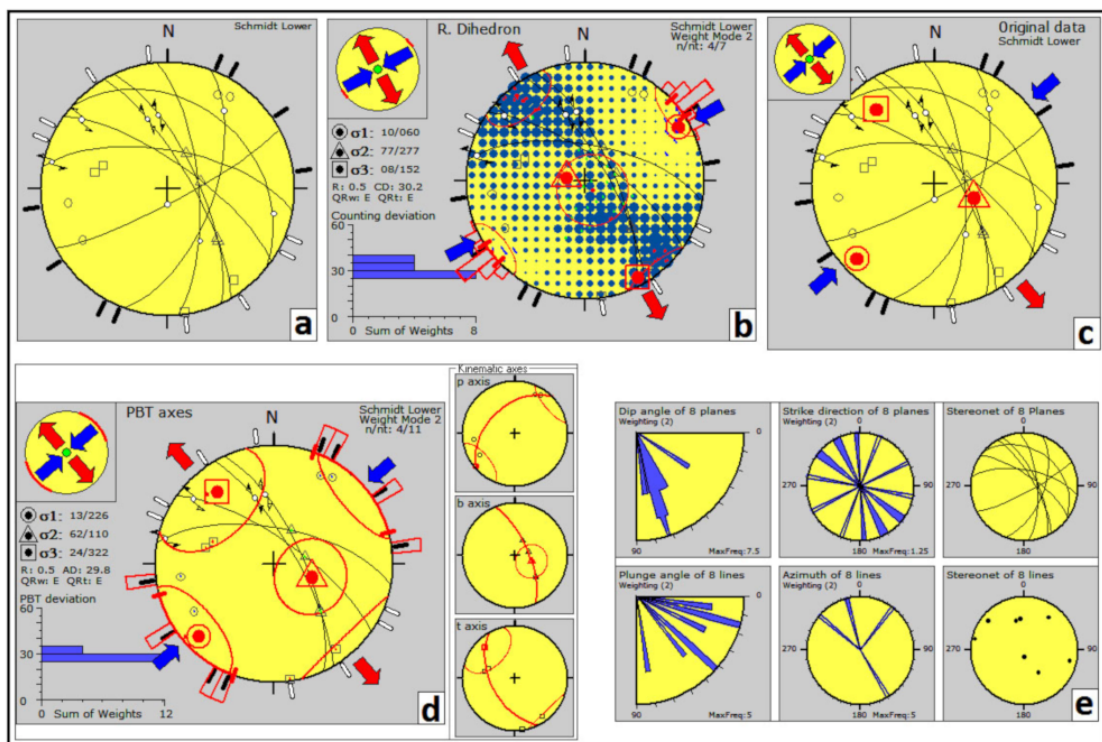


Figure 7. Cont.

Site 9



Site 26



**Figure 7.** Stress determination for upper Cretaceous units on site 17; Eocene units on site 20; Andesite and Dacite units of Oligocene on site 9; Quaternary units on site 26. (a) Stereoplot of faults. (b) Right Dihedron method. (c) Original data. (d) PBT axes method. (e) Rose diagram and stereonet of planes and lines. R: stress ratio, QRT: the tensor quality rank, QRw: quality rank for geological indicators,  $n/nt$ : ratio of fault-slip data used relative to the total number measured.

Igneous rocks were only observed on a few sites; however, those sites were scattered through the eastern part of the area (Figure 2). The geometric–kinematic data of the faults in the dacitic and andesitic units were separated from the other Eocene and Oligocene fault sets to determine why there were more dacitic and andesitic units in this area. Figure 8 shows images of these types of faults in the field. They had the appearance of normal faults with a strike-slip component. The value of the  $\Phi$  ratio was  $\sim 0.5$  at places where igneous units were exhumed, and the stress regime was transtensional because of local variations in stress regimes (Figure 6; Table 2). However, determining the stress regime for the study area required careful data separation, data analysis, and stress regime calculations. The determined stress tensors in sites 9 and 16 varied from the regional pattern of the state stress in the Oligocene. Three sites were situated adjacent to igneous units.

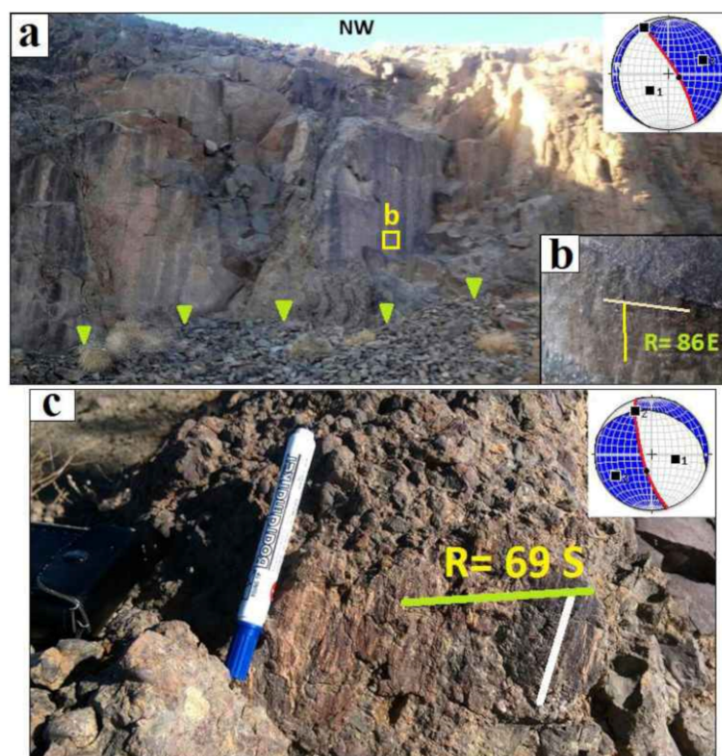


**Figure 8.** (a) Field photo of the F18 fault trace that is normal with a sinistral strike-slip component. (b) Slickenline on the minor fault in part. (c) Field photo of the F25 fault that is normal with a dextral component. Numbers 1, 2, and 3 in the stereonet indicate the orientation of the maximum, medium, and minimum stress axes, respectively.

Based on the results of the stress analysis, we deduced that local changes in the stress regimes from transpressional to transtensional were responsible for the outcropping of the igneous units in the eastern part of the Shekarab Mountains, where  $\sigma_1$  was vertical,  $\Phi$  was  $\sim 0.5$ , and the stress regime was transtensional. Therefore, the transtensional stress regime was responsible for the outcropping of Eocene igneous units in the study area's eastern part. The Miocene stress analysis indicated that the stress regime was strike-slip.

The brittle tectonic analysis showed different trends of compression, as shown by the reconstruction of the stress axes variations; consequently, the stress determination based on the direct inversion method revealed a variety of different trends of  $\sigma_1$  (Figure 6). Analysis of the brittle structure of the Shekarab Mountains revealed three major axes of minimum horizontal stress ( $\sigma_{hmin}$ ) running NE–SW, E–W, and NW–SE (Table 2). Furthermore, compression in the NW–SE trend was observed in the data gathered from the upper Cretaceous locations. On the other hand, the compressional stress regime in the area was consistent with five stress configurations. It was determined from the calculated data of the

five sites that the NE–SW  $\sigma_{\min}$  ( $\sigma_3$ ) and NW–SE  $\sigma_{\max}$  ( $\sigma_1$ ) directions of the paleostress fields accounted for 74% of the computed stress tensors.

As a result, the estimated averages of the three main stress axes were  $\sigma_1 = N290^\circ$ ,  $\sigma_2 = N192^\circ$ , and  $\sigma_3 = N026^\circ$ . The 0.3 value of  $\Phi$  confirmed that thrust faults and compressional stress regimes coexisted in this tectonic regime. In the second step of the stress regime, the N–S  $\sigma_{\max}$  ( $\sigma_1$ ) of the paleostress field was identified at 17 sites and accounted for 71% of the calculated stress tensors. The oriented mean stress axes of  $\sigma_1 = N035^\circ$ ,  $\sigma_2 = N126^\circ$ ,  $\sigma_3 = N304^\circ$ , and  $\Phi = 0.5$  further supported the coexistence of transpressive regimes in this tectonic regime. Six sites—10, 11, 23, 26, 28, and 29—were used to collect data for the Quaternary (Figures 6 and 9). The analysis of the data from site 26 is shown in Figure 7, where the stress regime was strike-slip, and the  $\sigma_1$  direction was toward NE–SW. At the six sites mentioned above, the NE–SW direction of  $\sigma_1$  in the paleostress field was found to account for 64% of the computed stress tensors. The principal stress axes of the estimated mean tensor were oriented as follows:  $\sigma_1 = N046^\circ$ ,  $\sigma_2 = N141^\circ$ ,  $\sigma_3 = N315^\circ$ , and  $\Phi = 0.5$ , indicating that this tectonic regime coexisted with strike-slip regimes. The configuration of the Shekarab Mountains was due to the three phases of Cenozoic deformation. Evidence of the different stress regimes is shown in Figure 10.

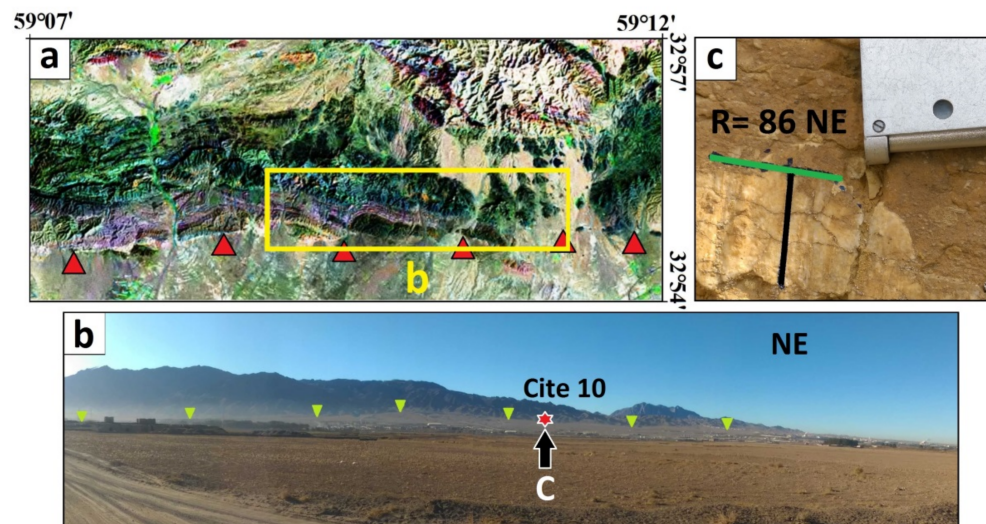


**Figure 9.** (a) Trace of North Birjand Fault (N.B.F) on the satellite image. (b) Field photo illustrating the location of the site 10. (c) Slickenline on the minor fault part.

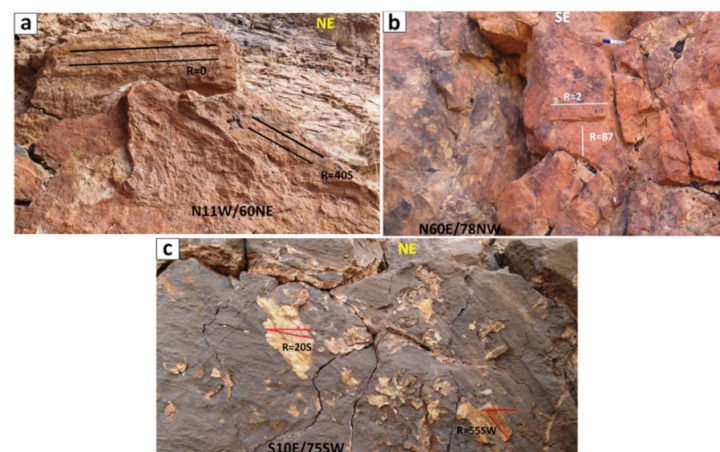


**Figure 10.** Field photo of the study area's faults in two different stress regimes: (a) dextral and reverse with a dextral component in site 18; (b) strike-slip with a normal component in volcanic rocks unit in site 16; (c) dextral with reverse component and normal with a dextral component in site 13.

### 3.2. Structural Analysis and Tectonic Pattern

Structural analysis of the complicated fault systems, using fault surface inversion methods, can cause complicated and often erroneously deduced histories of paleostress. Separating the fault kinematics data indicated the existence of three different major stress axis ( $\sigma_1$ ) directions, which represented three successive and discontinuous tectonic regimes. The earliest evidence of stress in the region dated back to the late Cretaceous. Compressive stress ( $\sigma_1 = N290^\circ$ ,  $\sigma_2 = N192^\circ$ ,  $\sigma_3 = N026^\circ$ , and  $\Phi = 0.3$ ) was operating in the study area during the late Cretaceous, as shown by the stress analyses, leading to the uplifting of ophiolites and peridotites in the eastern part of the area. The fault kinematics analysis in the Shekarab Mountains was used to infer the stress state during the Eocene. The fault-slip data collected at the nearby igneous units were normal with a strike-slip component. The principal stress axes were oriented as  $\sigma_1 = N035^\circ$ ,  $\sigma_2 = N126^\circ$ ,  $\sigma_3 = N304^\circ$ , and  $\Phi = 0.5$  during the second stress step (transpressive) in the Shekarab Mountains. Strike-slip was the third step of the stress regime in the area, with the principal stress axes oriented as  $\sigma_1 = N046^\circ$ ,  $\sigma_2 = N141^\circ$ ,  $\sigma_3 = N315^\circ$ , and  $\sim 0.5$ . Three distinct principal tectonic regimes were identified following kinematic and structural analyses of the faults formed during the late Cretaceous to the Quaternary. Inversion of fault-slip data collected from seven sites of Oligocene rocks indicated that the stress regime at this time was transpressional, and in two sites, 9 and 16, there were various stress regimes (transtensional). Regional changes in the stress regime from transpressional to transtensional in the eastern part of the study area indicated that the existence of different stress regimes has caused the emplacement of igneous rocks.

Rotations of stress fields are likely to occur over geological time. In many cases, these rotations are likely to be gradual and slow [49]. The fault datasets were used to infer stress field rotations from tectonic features and the paleostress history of the Shekarab Mountains. Every cluster of fault trends had a corresponding stress field orientation. Due to presence of various stress regimes in the area, multiple fault sets were formed by various stress regimes, accounting for a large portion of the detected complexity of the fault pattern in the Shekarab Mountains. There was a nearly  $80^\circ$  clockwise rotation of the stress field from the late Cretaceous to the Quaternary in the study area (Figure 11). The structural paleostress indicators showed that the orientation of brittle structures was in accord with the rotation of the paleostress (Figure 12). As deduced from earthquake fault surface solutions, the current maximum horizontal stress is oriented  $N025^\circ$  [47]. This trend agrees with the stress direction derived from deduced Quaternary fault kinematics.

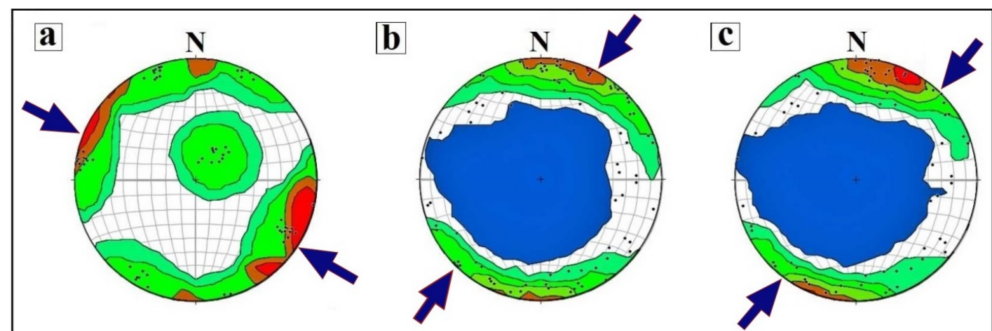


**Figure 11.** The  $\sigma_1$  orientations of density stereo plots for three paleostress fields were obtained: (a) late Cretaceous, (b) Eocene, and (c) Quaternary. The 1% contour intervals are represented in the southern hemisphere with equal-area projections.



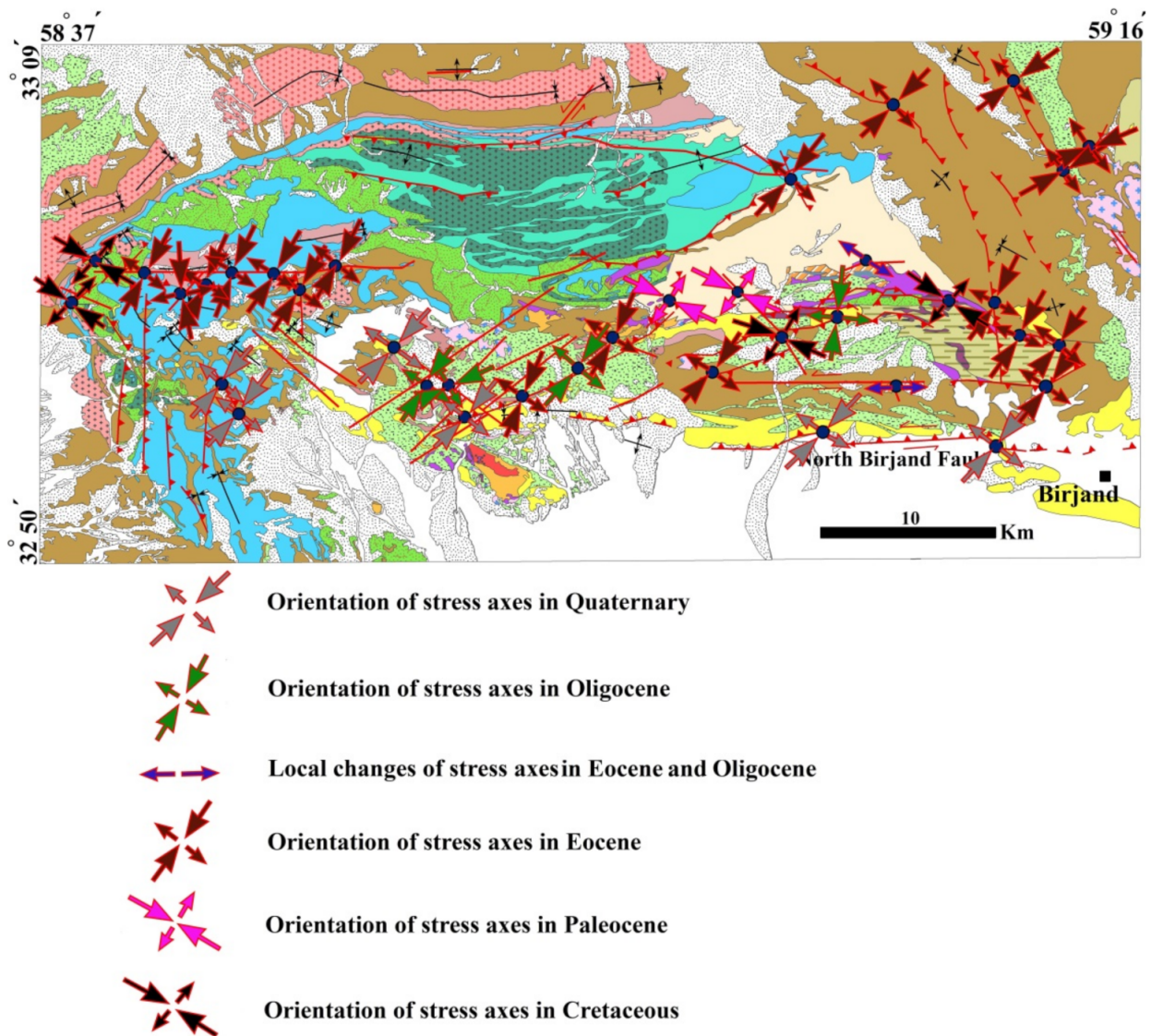


**Figure 12.** Directions of main stress axes in the study area from the late Cretaceous to Quaternary.

#### 4. Discussion

The fault slip data measured in the Pliocene–Quaternary conglomerates, where most of the data were collected, were analyzed to determine the current state of stress. Based on analysis of the maximum principal stress ( $\sigma_1$ ) direction and faults located in the different geological units, three successive episodes of deformation were recognized:

1. The oldest deformation stage was characterized by nearly E–W compression ( $N290^\circ$ ). It was documented in four outcrops (sites 13, 17, 32, and 33) with two compatible systems of reverse and strike-slip faults. To calculate the directions of stress axes in the Cretaceous, we removed faults in the Cretaceous with similar geometric–kinematic positions to Paleocene, Eocene, Oligocene, Pliocene, Miocene, and Quaternary faults in the dataset. Stress axes trends associated with the Cretaceous were obtained using the remaining faults with trends that were not similar to any of the faults related to the previous periods.

2. The second deformation stage was characterized by NE–SW direction compression ( $N035^\circ$ ). This stress axis direction was obtained using the Eocene and Oligocene strata. To determine stress axes directions in the Oligocene, fault data were collected from 6 outcrops (sites 9, 15, 16, 21, 24, and 25), faults were removed with geometric–kinematic positions (trends of the faults and rakes of the slickenlines) similar to those in the Pliocene, Miocene, and Quaternary faults, and the rest of the fault's stress axes direction was determined

in the Oligocene. To calculate the stress axes directions in the Eocene, fault data were collected from 19 outcrops (sites 1, 2, 3, 4, 5, 6, 7, 8, 12, 18, 20, 22, 27, 30, 31, 34, 35, 36, and 37), faults were separated from the primary fault dataset, Eocene fault data with similar geometric–kinematic positions to that in the Oligocene, Pliocene, Miocene, and Quaternary faults were removed, and stress axes directions related to the Eocene were obtained for the remaining faults.

3. The most recent episode is characterized by two systems of reverse and strike-slip faults consistently indicating an average  $N046^\circ$  direction of compression ( $\sigma_1$ ) found in 6 outcrops (sites 10, 11, 23, 26, 28, and 29). To obtain the direction of stress axes in the Quaternary, the faults related to this time were separated from all datasets and used to determine the stress tensors in the Quaternary.

The deviatoric stress tensors that were calculated and are associated with the current stress state of the SSZ deformation domains show a homogeneous stress field. The earthquake focal mechanisms analysis [50] conducted in the SSZ suggested that strike-slip faulting associated with the NE–SW direction of compression has been generated. Based on the inversion of earthquake focal mechanisms and geomorphic evidence, the present state of stress was analyzed by ref. [51]. These authors reported that the current  $\sigma_1$  direction is  $N030^\circ$ , which agreed with the axis of shortening inferred from the processing of GPS data [52]. The modern stress field was characterized in the  $N046^\circ$  " $\sigma_1$ " direction for almost all of the analyzed sites related to the Quaternary. Five of six sites, including sites 10, 11, 26, 28, and 29, indicated the  $\sigma_1$  direction to be the same as the regional stress state pattern (Table 2). However, the last site (site 23) showed a different and perturbed orientation from the regional modern stress state pattern. Site number 23 is situated at a two fault systems junction with NE–SW trending. The mean values of the  $\sigma_1$  axes with NE–SW orientation in the Quaternary, deduced from the kinematic analysis of the fault data, indicate a strike-slip regime and are in accordance with the vectors of GPS in the area. Figure 7 shows the trend of the maximum horizontal stress axes ( $\sigma_{hmax}$ ) of the current stress solutions.

The northward motion of Arabia with respect to Eurasia is controlling the active tectonics of Iran, as indicated by the current mean direction of  $\sigma_{hmax}$  ( $\sigma_1$ )  $\sim N010^\circ$ , measured by GPS motion relative to Arabia–Eurasia convergence [6,15,53]. The active subduction of the Arabian Plate below the Iranian micro-continent is visible on the surface of the Makran tectonic province [54]. However, the region is influenced by Makran subduction and Arabia–Eurasia collision. Kinematic and geometric data of structural features affected by these geodynamic processes indicate the present strike-slip regime of the Shekarab Mountains in eastern Iran. For the Quaternary, the mean direction of  $\sigma_1$  is NE–SW, and the stress regime is strike-slip. The value of  $\Phi$  obtained from the 37 sites was  $\sim 0.5$  in most locations (Table 2).

Some faults in the Shekarab Mountains only cut units related to certain geologic periods. For example, the F21 and F22 faults cut the Cretaceous units. Therefore, these faults were created because of the Cretaceous stress regime and were not reactivated by younger tectonic control. However, several tectonic regimes reactivated the F5 and F14 faults that cut the Paleocene, Eocene, Oligocene, Neogene, and Quaternary units. These faults occurred on rock units; hence, they were post-tectonic. Multiple-direction slickensides did not occur in a single phase of deformation, but were created during several stages of deformation. The presence of several slickensides on a single fault plane were due to changes in stress over time.

Inversion of the separate datasets helped to elucidate the significant changes in the direction of  $\sigma_1$ , including the NW–SE trend in the late Cretaceous, the nearly NE–SW direction in the Eocene, and the NE–SW direction in the Quaternary. Therefore, the direction of the major stress axis ( $\sigma_1$ ) has rotated in the Shekarab Mountains (Figures 11 and 12). This kind of interpretation related to stress field rotations has been used in various regions, including the Gabriel region, California [55]; Honduras [56]; Matanuska Valley, Alaska [57]; the Lake Mead fault system [49]; SE Chalkidiki, northern Greece [58]; and the San Andreas fault system located in southern California [59].

## 5. Conclusions

The inversion of distinct datasets enabled us to determine that the Shekarab Mountains have experienced occasional variations in stress regimes over time.

The separation of data based on fault kinematics revealed three continuous stress regimes in the study area. Inferred from analyses of fault kinematics, the  $\sigma_1$  direction is  $\sim$ N046° for the Quaternary stress state.

The Quaternary compression direction ( $\sigma_1$ ) roughly coincides with the current convergence direction between Arabia and Eurasia. Cretaceous and Quaternary stress tensors differed significantly, as shown by our analyses of brittle structures in the Shekarab Mountains. Our findings indicated that the compression direction ( $\sigma_1$ ) shifted from N290° during the Cretaceous–Paleocene, to N035° during the Eocene, and to N046° during the Oligocene to Quaternary.

Our compilation of paleostress data indicates that there have been different stress regimes in the study area: compression in the Cretaceous to Paleocene, transpression from Eocene to Oligocene, and strike-slip in the Quaternary. The results indicate that the stress regime's evolution corresponds to various tectonic events in the Shekarab Mountains. The stress states exhibited two distinct transtensional and transpressional tectonic regimes from the late Eocene to the Oligocene. Variations in the stress regime at sites 9 and 16 accounted for the transition from a homogenous (transpression) to heterogeneous (transtension) in the Eastern Shekarab Mountains. The information from sites 9 and 16 differed from the Oligocene stress state; in the eastern part of the area, regional shifts in stress regime from transpressional to transtensional caused the outcropping of volcanic rocks (andesite and dacite):

The initial phase of applied stress in the Shekarab Mountains was oblique thrusting, with the directions of the main stress axes being  $\sigma_1 =$  N290°,  $\sigma_2 =$  N192°, and  $\sigma_3 =$  N026° and the stress ratio = 0.3, which caused the uplift of ophiolites and peridotites.

The orientations of the principal stress axes in the second stage of transpressive stress were  $\sigma_1 =$  N035°,  $\sigma_2 =$  N126°, and  $\sigma_3 =$  N304° with a stress ratio = 0.5.

Strike-slip was the third step in the stress regime, with the main stress axes being  $\sigma_1 =$  N046°,  $\sigma_2 =$  N141°,  $\sigma_3 =$  N1315°, and  $\Phi =$  0.5.

**Author Contributions:** M.E.: formal analysis, methodology, fieldwork, investigation, writing the first draft of the manuscript; E.G. and A.R.: resources; methodology, validation, visualization, writing, review, and editing; E.G. and M.N.: conceptualization and design of the study, supervision, review, and editing; S.M.M., A.R. and M.N.: validation, visualization, supervision, review, and editing; S.S. and R.D.: visualization, supervision, writing, review, and editing. All authors contributed to the research and preparation of the manuscript and approved the submitted version. All authors have read and agreed to the published version of the manuscript.

**Funding:** This research received no external funding.

**Institutional Review Board Statement:** Not applicable.

**Informed Consent Statement:** Not applicable.

**Acknowledgments:** This work is the outcome of a joint research study with the University of Birjand, the International Institute of Earthquake Engineering and Seismology (IIEES), Shahid Bahonar University of Kerman, and Utrecht University (The Netherlands), whose participation in this study is gratefully acknowledged.

**Conflicts of Interest:** The authors declare no conflict of interest.

## References

1. Rashidi, A.; Derakhshani, R. Strain and Moment- Rates from GPS and Seismological Data in Northern Iran: Implications for an Evaluation of Stress Trajectories and Probabilistic Fault Rupture Hazard. *Remote Sens.* **2022**, *14*, 2219. [[CrossRef](#)]
2. Rashidi, A.; Khatib, M.M.; Derakhshani, R. Structural Characteristics and Formation Mechanism of the Earth Fissures as a Geohazard in Birjand, Iran. *Appl. Sci.* **2022**, *12*, 4144. [[CrossRef](#)]
3. Ghanbarian, M.A.; Derakhshani, R. The folds and faults kinematic association in Zagros. *Sci. Rep.* **2022**, *12*, 8350. [[CrossRef](#)] [[PubMed](#)]

4. Saccani, E.; Delavari, M.; Dolati, A.; Pandolfi, L.; Barbero, E.; Brombin, V.; Marroni, M. Geochemistry of volcanic rocks and dykes from the Remeshk-Mokhtarabad and Fannuj-Maskutan Ophiolites (Makran Accretionary Prism, SE Iran): New constraints for magma generation in the Middle East Neo-Tethys. *Geosyst. Geoenviron.* **2022**, 100140. [[CrossRef](#)]
5. Ezati, M.; Gholami, E. Neotectonics of the Central Kopeh Dagh drainage basins, NE Iran. *Arab. J. Geosci.* **2022**, *15*, 992. [[CrossRef](#)]
6. Vernant, P.; Nilforoushan, F.; Hatzfeld, D.; Abbassi, M.; Vigny, C.; Masson, F.; Nankali, H.; Martinod, J.; Ashtiani, A.; Bayer, R. Present-day crustal deformation and plate kinematics in the Middle East constrained by GPS measurements in Iran and northern Oman. *Geophys. J. Int.* **2004**, *157*, 381–398. [[CrossRef](#)]
7. Tirrul, R.; Bell, I.; Griffis, R.; Camp, V. The Sistan suture zone of eastern Iran. *Geol. Soc. Am. Bull.* **1983**, *94*, 134–150. [[CrossRef](#)]
8. Camp, V.; Griffis, R. Character, genesis and tectonic setting of igneous rocks in the Sistan suture zone, eastern Iran. *Lithos* **1982**, *15*, 221–239. [[CrossRef](#)]
9. Jentzer, M.; Whitechurch, H.; Agard, P.; Ulrich, M.; Caron, B.; Zarrinkoub, M.H.; Kohansal, R.; Miguet, L.; Omrani, J.; Fournier, M. Late Cretaceous calc-alkaline and adakitic magmatism in the Sistan suture zone (Eastern Iran): Implications for subduction polarity and regional tectonics. *J. Asian Earth Sci.* **2020**, *204*, 104588. [[CrossRef](#)]
10. Jackson, J.; McKenzie, D. Active tectonics of the Alpine—Himalayan Belt between western Turkey and Pakistan. *Geophys. J. Int.* **1984**, *77*, 185–264. [[CrossRef](#)]
11. Meyer, B.; Le Dortz, K. Strike-slip kinematics in central and eastern Iran: Estimating fault slip-rates averaged over the Holocene. *Tectonics* **2007**, *26*, 1–20. [[CrossRef](#)]
12. Walker, R.; Khatib, M. Active faulting in the Birjand region of NE Iran. *Tectonics* **2006**, *25*, 1–17. [[CrossRef](#)]
13. Şengör, A.; Altın, D.; Cin, A.; Ustaömer, T.; Hsü, K. Origin and assembly of the Tethyside orogenic collage at the expense of Gondwana Land. *Geol. Soc. Lond. Spec. Publ.* **1988**, *37*, 119–181. [[CrossRef](#)]
14. Rashidi, A.; Abbassi, M.-R.; Nilfouroushan, F.; Shafiei, S.; Derakhshani, R.; Nemati, M. Morphotectonic and earthquake data analysis of interactional faults in Sabzevaran Area, SE Iran. *J. Struct. Geol.* **2020**, *139*, 104147. [[CrossRef](#)]
15. Rashidi, A.; Khatib, M.M.; Nilfouroushan, F.; Derakhshani, R.; Mousavi, S.M.; Kianimehr, H.; Djamour, Y. Strain rate and stress fields in the West and South Lut block, Iran: Insights from the inversion of focal mechanism and geodetic data. *Tectonophysics* **2019**, *766*, 94–114. [[CrossRef](#)]
16. Baniadam, F.; Shabanian, E.; Bellier, O. The kinematics of the Dasht-e Bayaz earthquake fault during Pliocene-Quaternary: Implications for the tectonics of eastern Central Iran. *Tectonophysics* **2019**, *772*, 228218. [[CrossRef](#)]
17. Rashidi, A.; Kianimehr, H.; Shafieibafti, S.; Mehrabi, A.; Derakhshani, R. Active faults in the west of the Lut block (Central Iran). *Geophys. Res.* **2021**, *22*, 70–84. [[CrossRef](#)]
18. Nemati, M.; Derakhshani, R. Short-term seismicity patterns along the most active faults in Iran. *J. Iber. Geol.* **2021**, *47*, 441–459. [[CrossRef](#)]
19. Rahbar, R.; Shafiei Bafti, S.; Derakhshani, R. Investigation of the tectonic activity of Bazargan Mountain in Iran. *Sustain. Dev. Mt. Territ.* **2017**, *9*, 380–386. [[CrossRef](#)]
20. Kermani, A.F.; Derakhshani, R.; Bafti, S.S. Data on morphotectonic indices of Dashtekhak district, Iran. *Data Brief* **2017**, *14*, 782–788. [[CrossRef](#)]
21. Derakhshani, R.; Eslami, S. A new viewpoint for seismotectonic zoning. *Am. J. Environ. Sci.* **2011**, *7*, 212–218. [[CrossRef](#)]
22. Tadayon, M.; Rossetti, F.; Zattin, M.; Nozaem, R.; Calzolari, G.; Madanipour, S.; Salvini, F. The post-eocene evolution of the Doruneh Fault region (central Iran): The intraplate response to the Reorganization of the Arabia-Eurasia collision zone. *Tectonics* **2017**, *36*, 3038–3064. [[CrossRef](#)]
23. Jacques, A. Inversion of earthquake focal mechanisms to obtain the seismotectonic stress IV—A new method free of choice among nodal planes. *Geophys. J. Int.* **2002**, *150*, 588–609. [[CrossRef](#)]
24. Diabat, A.A.; Atallah, M.; Salih, M.R. Paleostress analysis of the Cretaceous rocks in the eastern margin of the Dead Sea transform, Jordan. *J. Afr. Earth Sci.* **2004**, *38*, 449–460. [[CrossRef](#)]
25. Baroň, I.; Kernstocková, M.; Faridi, M.; Bubík, M.; Milovský, R.; Melichar, R.; Sabouri, J.; Babůrek, J. Paleostress analysis of a gigantic gravitational mass movement in active tectonic setting: The Qoshadagh slope failure, Ahar, NW Iran. *Tectonophysics* **2013**, *605*, 70–87. [[CrossRef](#)]
26. Ezati, M.; Azizzadeh, M.; Riahi, M.A.; Fattahpour, V.; Honarmand, J. Characterization of micro-fractures in carbonate Sarvak reservoir, using petrophysical and geological data, SW Iran. *J. Pet. Sci. Eng.* **2018**, *170*, 675–695. [[CrossRef](#)]
27. Ezati, M.; Azizzadeh, M.; Riahi, M.A.; Fattahpour, V.; Honarmand, J. Application of DSI log in geomechanical and petrophysical evaluation of carbonate reservoirs: A case study in one of the SW Iranian oil fields. *J. Pet. Res.* **2019**, *29*, 37–50. [[CrossRef](#)]
28. Li, D.; McGuire, J.J.; Liu, Y.; Hardebeck, J.L. Stress rotation across the Cascadia megathrust requires a weak subduction plate boundary at seismogenic depths. *Earth Planet. Sci. Lett.* **2018**, *485*, 55–64. [[CrossRef](#)]
29. Van Nguyen, V.; Hoai, L.T.T. Cenozoic paleostress evolution in south central Vietnam: Implication for changing dynamics of faulting along the eastern Indochina continental margin. *J. Asian Earth Sci.* **2019**, *185*, 104006. [[CrossRef](#)]
30. Žaba, J.; Gaidzik, K. Variscan stress regime rotation: Insights from the analysis of kink folds in the northern margin of the Bohemian Massif, South Poland. *Comptes Rendus Geosci.* **2019**, *351*, 395–405. [[CrossRef](#)]
31. Xu, S.; Liu, R.; Hao, F.; Engelder, T.; Yi, J.; Zhang, B.; Shu, Z. Complex rotation of maximum horizontal stress in the Wufeng-Longmaxi Shale on the eastern margin of the Sichuan Basin, China: Implications for predicting natural fractures. *Mar. Pet. Geol.* **2019**, *109*, 519–529. [[CrossRef](#)]

32. Tadayon, M.; Rashid, H.; Salehi, M.A.; Aslani, A. Post-Cretaceous structural reconstruction of the west Central Iranian micro-plate: Insights from structural and magnetic fabrics (AMS) constraints. *J. Struct. Geol.* **2022**, *160*, 104601. [[CrossRef](#)]
33. Biswas, T.; Bose, N.; Dutta, D.; Mukherjee, S. Arc-parallel shears in collisional orogens: Global review and paleostress analyses from the NW Lesser Himalayan Sequence (Garhwal region, Uttarakhand, India). *Mar. Pet. Geol.* **2022**, 105530. [[CrossRef](#)]
34. Freund, R. Rotation of strike slip faults in Sistan, southeast Iran. *J. Geol.* **1970**, *78*, 188–200. [[CrossRef](#)]
35. Berberian, M.; Yeats, R.S. Patterns of historical earthquake rupture in the Iranian Plateau. *Bull. Seismol. Soc. Am.* **1999**, *89*, 120–139. [[CrossRef](#)]
36. Jackson, J.; Haines, J.; Holt, W. The accommodation of Arabia-Eurasia plate convergence in Iran. *J. Geophys. Res. Solid Earth* **1995**, *100*, 15205–15219. [[CrossRef](#)]
37. Ezati, M.; Gholami, E.; Mousavi, S.M. Tectonic activity level evaluation using geomorphic indices in the Shekarab Mountains, Eastern Iran. *Arab. J. Geosci.* **2021**, *14*, 385. [[CrossRef](#)]
38. Ezati, M.; Gholami, E.; Mousavi, S.M.; Rashidi, A.; Derakhshani, R. Active Deformation Patterns in the Northern Birjand Mountains of the Sistan Suture Zone, Iran. *Appl. Sci.* **2022**, *12*, 6625. [[CrossRef](#)]
39. Khatib, M. Structural Analysis of Southern Birjand Mountains. Ph.D. Thesis, Shahid Beheshti University, Tehran, Iran, 1998.
40. Angelier, J. Tectonic analysis of fault slip data sets. *J. Geophys. Res. Solid Earth* **1984**, *89*, 5835–5848. [[CrossRef](#)]
41. Angelier, J. Inversion of field data in fault tectonics to obtain the regional stress—III. A new rapid direct inversion method by analytical means. *Geophys. J. Int.* **1990**, *103*, 363–376. [[CrossRef](#)]
42. Angelier, J.T.; Mechler, P. Sur une methode graphique de recherche des contraintes principales egalement utilisables en tectonique et en seismologie: La methode des diedres droits. *Bull. Soc. Géol. Fr.* **1977**, *7*, 1309–1318. [[CrossRef](#)]
43. Bott, M.H.P. The mechanics of oblique slip faulting. *Geol. Mag.* **1959**, *96*, 109–117. [[CrossRef](#)]
44. Wallace, R.E. Geometry of shearing stress and relation to faulting. *J. Geol.* **1951**, *59*, 118–130. [[CrossRef](#)]
45. Hippolyte, J.-C.; Bergerat, F.; Gordon, M.B.; Bellier, O.; Espurt, N. Keys and pitfalls in mesoscale fault analysis and paleostress reconstructions, the use of Angelier's methods. *Tectonophysics* **2012**, *581*, 144–162. [[CrossRef](#)]
46. Carey, E. Recherche des directions principales de contraintes associées au jeu d'une population de failles. *Rev. Géogr. Phys. Géol. Dyn.* **1979**, *21*.
47. Jentzer, M.; Fournier, M.; Agard, P.; Omrani, J.; Khatib, M.M.; Whitechurch, H. Neogene to Present paleostress field in Eastern Iran (Sistan belt) and implications for regional geodynamics. *Tectonics* **2017**, *36*, 321–339. [[CrossRef](#)]
48. Delvaux, D.; Sperner, B. Stress tensor inversion from fault kinematic indicators and focal mechanism data: The TENSOR program. *New Insights Struct. Interpret. Model.* **2003**, *212*, 75–100.
49. Ron, H.; Nur, A.; Aydin, A. Stress field rotation or block rotation: An example from the Lake Mead fault system. *Ann. Geophys.* **1993**, *36*.
50. Dziewonski, A.M.; Chou, T.A.; Woodhouse, J.H. Determination of earthquake source parameters from waveform data for studies of global and regional seismicity. *J. Geophys. Res. Solid Earth* **1981**, *86*, 2825–2852. [[CrossRef](#)]
51. Shabanian, E.; Bellier, O.; Abbassi, M.R.; Siame, L.; Farbod, Y. Plio-quadernary stress states in NE Iran: Koppeh Dag and Allah Dag-Binalud mountain ranges. *Tectonophysics* **2010**, *480*, 280–304. [[CrossRef](#)]
52. Masson, F.; Chéry, J.; Hatzfeld, D.; Martinod, J.; Vernant, P.; Tavakoli, F.; Ghafory-Ashtiani, M. Seismic versus aseismic deformation in Iran inferred from earthquakes and geodetic data. *Geophys. J. Int.* **2005**, *160*, 217–226. [[CrossRef](#)]
53. Ezati, M.; Gholami, E.; Mousavi, S.M. Paleostress regime reconstruction based on brittle structure analysis in the Shekarab Mountain, Eastern Iran. *Arab. J. Geosci.* **2020**, *13*, 1232. [[CrossRef](#)]
54. Burg, J.-P. Geology of the onshore Makran accretionary wedge: Synthesis and tectonic interpretation. *Earth-Sci. Rev.* **2018**, *185*, 1210–1231. [[CrossRef](#)]
55. Terres, R.R.; Luyendyk, B.P. Neogene tectonic rotation of the San Gabriel region, California, suggested by paleomagnetic vectors. *J. Geophys. Res. Solid Earth* **1985**, *90*, 12467–12484. [[CrossRef](#)]
56. Manton, W. Tectonic interpretation of the morphology of Honduras. *Tectonics* **1987**, *6*, 633–651. [[CrossRef](#)]
57. Stamatakos, J.A.; Kodama, K.; Pavlis, T.L. Paleomagnetism of Eocene plutonic rocks, Matanuska Valley, Alaska. *Geology* **1988**, *16*, 618–622. [[CrossRef](#)]
58. Pavlides, S.; Kiliass, A. Neotectonic and active faults along the Serbomacedonian zone (SE Chalkidiki, northern Greece). *Ann. Tecton.* **1987**, *1*, 97–104.
59. Nicholson, C.; Seeber, L.; Williams, P.; Sykes, L.R. Seismic evidence for conjugate slip and block rotation within the San Andreas fault system, southern California. *Tectonics* **1986**, *5*, 629–648. [[CrossRef](#)]